Electro-thermal poling in bioactive sodium-calcium phosphate-silicate glass: Anodic near-surface network connectivity changes and second harmonic generation

D. Palles, M. Marc Dussauze, C.R. Mariappan, V. Rodriguez, B. Roling, E.I. Kamitsos

17 (2023) 100164

Contents lists available at ScienceDirect

Journal of Non-Crystalline Solids: X

journal homepage: www.sciencedirect.com/journal/journal-of-non-crystalline-solids-x

Electro-thermal poling in bioactive sodium-calcium phosphate-silicate glass: Anodic near-surface network connectivity changes and second harmonic generation

D. Palles [a], M. Dussauze [b], C.R. Mariappan [c], V. Rodriguez [b], B. Roling [c], E.I. Kamitsos [a,*]

[a] Theoretical and Physical Chemistry Institute, National Hellenic Research Foundation, 48 Vassileos Constantinou Ave., Athens 11635, Greece
[b] Institut des Sciences Moleculaires - UMR 5255 CNRS, Université Bordeaux, Talence Cedex, France
[c] Department of Chemistry, University of Marburg, Hans-Meerwein-Strasse 4, Marburg 35032, Germany

ARTICLE INFO

Keywords:
Phosphate-silicate bioglasses
Electro-thermal poling
Raman spectroscopy
Second harmonic generation
Network connectivity

ABSTRACT

We report Raman spectra in the sub-anodic region after electro-thermal poling of the 46S4 bioglass and show a correlation between structural changes and the induced second harmonic generation (SHG). The Raman peak at ca. 625 cm^{-1}, due to the symmetric stretching-bending vibration of Si-O-Si bridges, was employed to quantify the poling-induced structural changes since its frequency ν_s(Si-O-Si) varies linearly with the silicate network connectivity, NC. Key results include the increase of network connectivity towards the anode after poling, with NC varying from 2.24 before poling to 2.37 at the anode after poling. SHG measurements showed the presence of an optically-inactive layer of 1.0 μm thick below the anode, followed by an optically-active layer where the SHG signal is maximized from about 1.5 to 4.0 μm. In this layer the NC takes intermediate values and reflects modest changes with respect to the pristine bioglass. The present findings suggest that the transport of electrons near the metal film anode is faster than the Na ion transport towards the cathode.

1. Introduction

Electro-thermal poling (ETP) of glasses involves the post-synthesis application of a dc voltage, V_p, ranging from a few tens of V up to a few kV/mm, together with a mild thermal treatment below the glass transition temperature for sufficient time to reach a steady state. This process is followed by cooling the sample to room temperature while keeping the field on and then switching off the bias voltage. After its original application to silica glass and the achievement of poling-induced second order non-linearity [1], ETP has been used for a variety of glass applications. The request to enhance second order non-linear properties like Second Harmonic Generation (SHG) by tailoring appropriate glass compositions and poling conditions has led to studies in a broad area ranging from glasses with high SHG [2,3] to anodic bonding in microelectronics [4]. In the field of bioactive glasses, interest in ETP poling has grown after the observation that this treatment accelerates the formation of bone-like apatite [5–8]. Electro-thermal imprinting in glasses and glass-metal nanocomposites has been proposed as an alternative type of lithography/patterning appropriate for the production of low-cost diffraction or other structures on the surface of metal-film-covered glasses [9,10]. Electric field-induced softening (EFIS) has been suggested as an innovative energy-saving glass-processing technique bearing similarities with ETP [11,12]; with EFIS including phenomena with activation energies ranging up to about one order of magnitude higher than the ones encountered in standard ETP poling. Additional applications of ETP include the alteration of surface wetting [13], reactivity [14], the surface electrical properties [10,15] as well as the mechanical properties of glasses [16,17].

The chemical and physical processes at play during ETP poling have been the subject of a significant amount of literature involving research from diverse fields like physical chemistry, optics, spectroscopy and materials science, based on a series of characterization techniques. Various compositions of thermally poled glasses with different admixtures of glass formers and modifiers have been studied, and modelling of the mechanisms describing the main processes has been presented for glasses including potassium niobium-silicate [18], soda-lime silicate [19–21], borosilicate [22,23], borate [24], borophosphate [25], aluminophosphate [26] and germanate [27] glasses.

After clear experimental evidence obtained originally by Carlson et al. for silicate glasses [28–31], and by others for a range of

* Corresponding author.
E-mail address: eikam@eie.gr (E.I. Kamitsos).

https://doi.org/10.1016/j.nocx.2023.100164
Received 20 December 2022; Received in revised form 5 February 2023; Accepted 14 February 2023
Available online 16 February 2023

multicomponent glasses [2,3,19–27], the consensus is that an electric-field-induced mobile cation depletion layer is created at the anode side of the poled glass, with structure and composition different from that of the pristine unpoled glass. Depending on the anode electrode configuration (i.e., open versus fully blocking), the cation deficit is compensated either by injection of positively charged species of atmospheric origin (H_3O^+/H^+) or by the drift of negatively charged carriers. The nature and the mobility of these carriers is at the origin of the apparently different proposed mechanisms; they can be grouped in two main categories: anionic (i.e. oxygen) conduction or electronic conduction [see Ref. 2 for a review]. One way to reconcile the two mechanisms is to consider that both anions and electrons contribute to the charge compensation through oxidation reactions forming neutral species while releasing electrons, while the glass composition determines which charge compensation path is the most preferable during thermal poling. In the case of ionic glasses, the negatively charged carriers that initiate the changes are the non-bridging oxygen atoms, and there is evidence for a glass-structure rearrangement in the sub-anodic region through conversion to bridging oxygen atoms (i.e., the glass connectivity increases) and the concomitant formation of molecular oxygen. Investigations on soda-lime silicates [20] have focused on the anodic surface nanoscale relief formation at the contact area between the glass and the anode electrode. The relief increases linearly as a function of the thermal poling charge density because of these structural changes, until it saturates and creates voids and cracks since the glass approaches its breakdown limit. The relief creation has been interpreted as a glass volume "shrinkage" resulting from the combination of the cation-exchange with H_3O^+/H^+ and the glass rearrangements. In another study [21], evidence was presented for molecular oxygen formation appearing maximal in the anodic surface craters formed because of poling current inhomogeneities, and the non-bridging oxygen recombination was proposed as key mechanism for interstitial oxygen formation. Recent molecular dynamics simulations of the ion migration and structural reorganization processes in electro-thermally poled borosilicate and aluminosilicate glasses [32,33] and borate glasses [34] have reproduced the main experimental trends seen in different glass systems and poling configurations. They include the conversion of negatively charged structural units into neutral ones in the charge depletion region, which leads to the increased polymerization of the network close to the anodic surface [32–34], the generation of free oxygen species and the establishment of an internal electric field [34].

In situ impedance spectroscopy and poling current measurements on the 46S4 bioglass during ETP poling, and ion concentration profiling after ETP poling, give a detailed picture of the kinetics and the time scales of two distinct charge compensation mechanisms leading to the anode/cathode layer formation [35–37]. With poling conditions V_p = 50 V and T_p = 200 °C, a double layer formation at the glass–anode interface was detected, involving a Na^+/Ca^{2+} depletion layer followed by a second Ca^{2+} pile-up layer of similar thickness (ca. 50 nm each).

Here we use more intense ETP poling conditions (V_p = 1500 V, T_p = 200 °C, poling time 45 min), and fully blocking electrodes to ensure attainment of a steady state on the same 46S4 bioglass of the previous studies [35–37] and focus on the depth dependence of the structural changes at the anode side, as probed by micro-Raman spectroscopy. Structural changes are quantified in terms of the glass network connectivity, and are correlated with the measured ETP-induced second harmonic generation signal. Before addressing the poling-induced changes in the 46S4 bioglass, we have considered glasses in the Na-, Ca- and mixed (Na + Ca)-silicate families for which we have demonstrated linear correlations between the Raman frequency of the symmetric stretching-bending vibration of the Si-O-Si bridges, ν_s(Si-O-Si), and the silicate network connectivity, NC. This allowed for the quantification of the depth dependence of network connectivity after electro-thermal poling by Raman spectroscopy. To facilitate the presentation of this work, we organize and discuss the results in two parts; the first part deals with the structure of the pristine 46S4 bioglass and related Na- and Ca-silicate glass families, while the ETP-induced sub-anodic structural changes and SHG are included in the second part of this study.

2. Experimental

The 46S4 bioglass with composition 25.2Na_2O-25.2CaO-3.2P_2O_5–46.4SiO_2 (in mol%) was synthesized from SiO_2, Na_2CO_3, $CaCO_3$ and $(NH_4)_2HPO_4$ powders as described previously [35]. The 46S4 samples were subsequently annealed, cut and polished in the form of cylindrical discs of ca. 10 mm diameter and sub 1 mm thickness, and finally sputtered on both faces with Pt for ETP poling experiments. The 46S4 sample that was thermally poled, at V_p = 1500 V and T_p = 200 °C for 45 min, was used for the micro-SHG and micro-Raman measurements.

For SHG and Raman measurements, the sample was cut approximately along the disk diameter and measurements were performed on the freshly cut surface as a function of distance from the anode side. The micro-Raman and micro-SHG measurements were carried out in the backscattering geometry in a modified Raman system (HR800 Horiba/Jobin-Yvon), equipped with an automated xyz stage using two aligned laser beams at 1064 nm and 532 nm as described elsewhere [38]. The micro-Raman linescans or maps were done first on a selected sample area using the 532 nm line, and then the micro-SHG measurements were run on the same sample area using for excitation the 1064 nm line of a Nd:yttrium aluminum garnet (Nd:YAG) EKSPLA picosecond laser (λ = 1064 nm, 2 kHz, 65 ps pulses) with a typical energy <50 μJ. The linescan or map step was set to 0.5 μm and a 100× objective with a numerical aperture of 0.5 was used; the combined effect is a spatial resolution better than 1 μm.

3. Results and discussion

3.1. On the structure of pristine bioglass 46S4 and related silicate glass families

Before discussing the poling-induced structural changes, we consider first the structural characteristics of the 46S4 bioglass. This glass can be described as a network of corner-sharing SiO_4 tetrahedra with a substantial amount of non-bridging oxygens as dictated by its quasi meta-silicate composition. The silicate non-bridging oxygens are charge-balanced through mainly ionic bonding by the sodium and the calcium ions. The small amount of phosphate (3.2 mol% P_2O_5) is expected to be dispersed as isolated ortho-phosphate tetrahedra, PO_4^{3-}, which also are charged-balanced by the alkali and alkaline earth ions. In fact, P_2O_5 is known to be more acidic than SiO_2 with $\Lambda(P_2O_5) = 0.40$ and $\Lambda(SiO_2) = 0.48$, where Λ is the optical basicity [39] and, thus, the modification and charge-balancing of the phosphate species by the modifier cations is expected to occur before that of the silicate network.

Since the composition of the 46S4 glass is close to the meta-silicate stoichiometry (50 mol% glass modifier oxide – 50 mol% SiO_2), one would expect that the majority of the silicate tetrahedra would have two non-bridging oxygens, i.e. Q^2_{Si} species. Modifier ions having different field strengths (charge/ionic radius), combined with the small phosphate fraction and the preparation conditions, are expected to result in the so-called disproportionation reaction, described in Eq. (1). This chemical equilibrium between different Q^n_{Si} species, where Q^n_{Si} denotes a silicate tetrahedron with n bridging oxygen atoms (n = 4, 3, 2, 1), may shift according to the field strength of the charge-balancing cation:

$$2Q^2{}_{Si} \rightleftharpoons Q^3{}_{Si} + Q^1{}_{Si} \quad (1)$$

A useful parameter to quantify the degree of cross-linking of the silicate network in the presence of a small quantity of P_2O_5 is the silicate network connectivity, NC, calculated by:

$$NC = \frac{4[SiO_2] + 6[P_2O_5] - 2([M_2O] + [M'O])}{[SiO_2]} \quad (2)$$

where [SiO_2], [P_2O_5], [M_2O] and [M'O] are the oxide contents in mol%, with the above expression being applicable also to purely silicate glasses [40]. NC is essentially the average number of bridging oxygens per SiO_4 tetrahedron after consumption of the modifier cations needed to charge-balance all the phosphate species, which are assumed to be present as orthophosphate units, PO_4^{3-} [40].

Solid state ^{29}Si and ^{31}P Nuclear Magnetic Resonance (NMR) spectroscopy results on the very similar bioglasses 45S5 and 46S2.6, i.e. 24.4Na_2O-26.9CaO-2.6P_2O_5–46.1SiO_2 [41] and 24.6Na_2O-26.7CaO-2.6P_2O_5–46.1SiO_2 [42] (mol%), respectively, have yielded the silicate and phosphate speciation given in Table 1. The NMR results show that these glasses have very similar connectivity (NC(45S5) = 2.12, NC (S462.6) = 2.14) which is very close to that predicted from Eq. (2) (NC = 2.12). Also, the phosphate speciation ($Q_P^0 \approx 100$) confirms the assumption for the presence of orthophosphate PO_4^{3-} species, while the coexistence of Q_{Si}^n silicate species with $n = 3$, 2 and 1 is in line with the chemical equilibrium expressed by Eq. (1).

The Raman spectra of bulk bioglasses should in principle be in line with the above considerations. To verify this assumption we compare in Fig. 1 the measured Raman spectrum of the 46S4 bioglass with the spectra reproduced from the literature for the bioglass compositions 60S3.8, 55S4.3 and 45S5 [43,44], and for the binary $x$$Na_2O$-(1–$x$)$SiO_2$ glasses with $x = 0.33$, 0.40, 0.45 [45] and $x = 0.50$ [46]. The two main features of the Raman spectrum of the pristine 46S4 glass (Fig. 1) are (a) an intense envelope at about 800–1200 cm^{-1} comprising a peak centered at 948 cm^{-1}, a broad shoulder at about 1055 cm^{-1} and a lower intensity peak at ca. 868 cm^{-1}, and (b) another intense and asymmetric band envelope centered at 625 cm^{-1}. Furukawa et al. [49] attributed the latter band in modified silicate glasses to the symmetric stretching-bending vibration of the Si-O-Si bridges, ν_s(Si-O-Si), and observed that it upshifts with increasing network depolymerization, i.e. upon increasing the number of non-bridging oxygen (NBO) atoms per silicate tetrahedron. Fig. 1 shows that the ca. 625 cm^{-1} band is asymmetric at its higher frequency side due to the presence of a variety of Si-O-Si bridges between Q_{Si}^4, Q_{Si}^3, Q_{Si}^2 and Q_{Si}^1 units [50]. A density functional theory study of the vibrational properties of sodium tetra-, tri- and di-silicate glasses has also attributed the increase of the ν_s(Si-O-Si) frequency to the increasing number of NBOs at higher sodium contents [51], which causes the shifting of the distribution of the inter-tetrahedral Si-O-Si angles to lower values.

To facilitate comparison, Fig. 1 presents side by side the Raman spectra of bioglasses and of the binary Na-silicate glasses having the closest available composition. For this purpose, we evaluated for bioglasses the effective SiO_2 content, $(1–x)_{Si}^{eff}$, after consideration of the amount of metal oxide modifiers needed to convert all P ions to orthophosphate tetrahedra:

$$(1–x)_{Si}^{eff} = [SiO_2]/\{[SiO_2] + [Na_2O] + [CaO] – 3[P_2O_5]\} \quad (3)$$

In the above expression, the factor of 3[P_2O_5] is subtracted from the total oxide modifier content, [Na_2O] + [CaO], to account for the formation of PO_4^{3-} anions. Apart from $(1–x)_{Si}^{eff}$, Table 2 compares values for NC, P/Si and [Na_2O] + [CaO] contents between bio-glasses and the corresponding binary Na-silicate glasses. For example, the deviations of NC and $(1–x)_{Si}^{eff}$ for bioglass 45S5 from the pure metasilicate composition (NC = 2.0) are of the order of 5.5% [=(2.11–2.0)/2.0] and 3% [=(0.515–0.50)/0.50], respectively.

Table 1
NMR results for the populations of Q^n species (mol%) for bioglasses 45S5 [41] and 46S2.6 [42]. Q_{Si}^n and Q_P^n indicate silicate and phosphate tetrahedra with n bridging oxygen atoms.

Bioglass	Q_{Si}^3	Q_{Si}^2	Q_{Si}^1	Q_P^1	Q_P^0
45S5	22.3	67.2	10.5	~0	~100
46S2.6	21	72	7	4.1	95.9

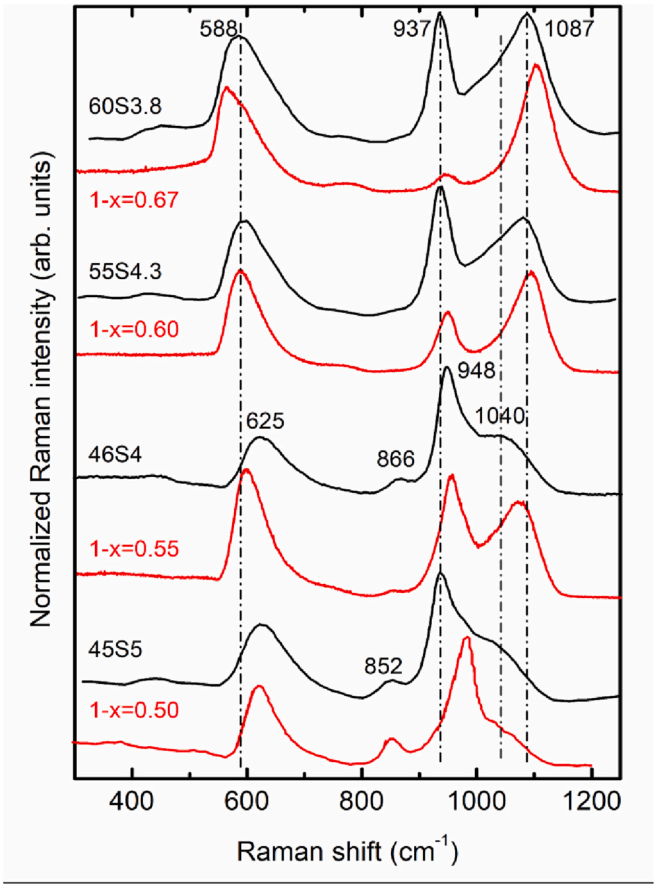

Fig. 1. Raman spectrum measured for bioglass 46S4 and spectra reproduced from the literature for other bioglasses [43,44,47,48] and for binary Na-silicate glasses $x$$Na_2O$-(1–$x$)$SiO_2$ with x = 0.33, 0.40, 0.45 [45] and x = 0.50 [46] of similar connectivity.

Table 2
Selected bioglasses and corresponding binary $x$$Na_2O$-(1–$x$)$SiO_2$ glasses used for Raman comparison in Fig. 1. Note the similarity in values for silicate network connectivity, NC, and SiO_2 content, $(1–x)_{Si}^{eff}$, for each pair of bioglass and binary sodium-silicate glass.

Bioglass name and composition Na-silicate glass of similar connectivity	NC	P/Si	$(1–x)_{Si}^{eff}$	Na_2O + CaO
60S3.8: 0.177Na_2O-0.196CaO- 0.026P_2O_5–0.601SiO_2	3.02	0.087	0.671	0.373
0.333Na_2O-0.667SiO_2	3.00	0	0.667	0.333
55S4.3: 0.201Na_2O-0.222CaO- 0.026P_2O_5–0.551SiO_2	2.75	0.094	0.615	0.423
0.40Na_2O-0.60SiO_2	2.67	0	0.600	0.400
46S4: 0.252Na_2O-0.252CaO- 0.032P_2O_5–0.464SiO_2	2.24	0.138	0.532	0.504
0.45Na_2O-0.55SiO_2	2.36	0	0.55	0.45
45S5: 0.244Na_2O-0.269CaO- 0.026P_2O_5–0.461SiO_2	2.11	0.113	0.515	0.513
0.50Na_2O-0.50SiO_2	2.00	0	0.50	0.50

3.1.1. *Medium frequency Raman region*

All the features of the pristine 46S4 Raman spectrum in Fig. 1 are generally in agreement with previously published data on similar bioglasses [43,44,47,48], while variations in band positions and relative intensities can originate from differences in composition and sample thermal history. The ν_s(Si-O-Si) frequency, as obtained by the first derivative method illustrated in Fig. 7 of section 3.2 for the poled bioglass 46S4, was found to exhibit an approximately linear decrease with increasing silicate network connectivity as illustrated in Fig. 2 for the

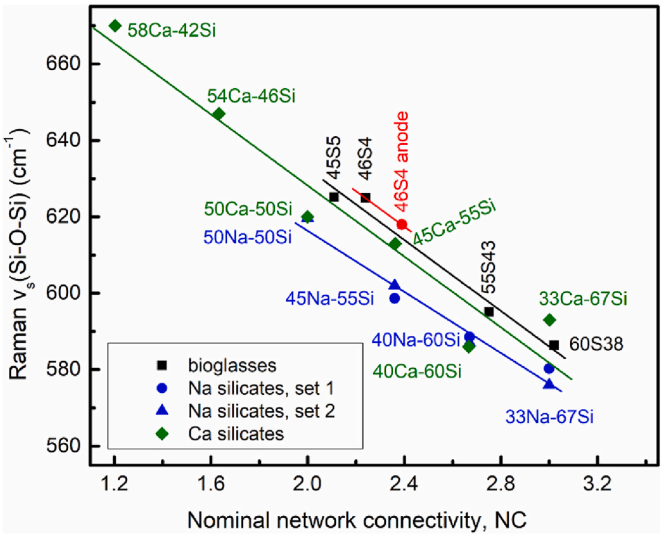

Fig. 2. The Raman frequency ν_s(Si-O-Si) as a function of the nominal silicate connectivity, NC, for bioglasses [43,44,47,48] and for binary Na-silicate (set1: Ref. 45, set2: Ref. 46) and Ca-silicate [52] glasses xMO-(1–x)SiO_2 (M = Na_2 or Ca) of similar connectivity. The v_s(Si-O-Si) frequencies were obtained by the first derivative method illustrated in Fig. 7 for the poled bioglass 46S4. Straight lines represent linear fits to the data for pristine bioglasses (black line) and for Ca-silicate (green line) and Na-silicate (blue line) glasses. (For interpretation of the references to colour in this figure legend, the reader is referred to the web version of this article.)

spectra shown in Fig. 1, and also for ν_s(Si-O-Si) data obtained in this work from reported spectra of binary Ca-silicate glasses [52]. Linear fits for the 3 glass families (bioglasses, Ca- and Na-silicate glasses) give the dependence of the ν_s(Si-O-Si) frequency (in cm^{-1}) on the network connectivity, NC:

$$\nu_s(\mathrm{Si-O-Si}) = a - b\,NC \quad (4)$$

where the fitting parameters take the values: (i) bioglasses: a = 725.8 ± 12.5 cm^{-1}, b = 46.6 ± 4.9 cm^{-1}, (ii) Ca-silicates: a = 721.2 ± 14.0 cm^{-1}, b = 46.5 ± 6.3 cm^{-1}, and (iii) Na-silicates: a = 696.5 ± 8.8 cm^{-1}, b = 40.0 ± 3.4 cm^{-1}. The results show that the intercept and slope of the bioglass series are very close to those of the binary Ca-silicate data, providing evidence for the role of Ca^{2+} ions in dictating the behavior of bioglasses.

The dependence of the ν_s(Si-O-Si) frequency on NC can be understood to result from the increasing number of NBOs at higher modifier contents, which leads to lower NC and the shifting of the inter-tetrahedral Si-O-Si angle to lower values [51]. The higher ν_s(Si-O-Si) frequency values of the bioglass series compared to Na-silicate glasses of the same NC value are probably related to the difference in the ionic field strength between Ca^{2+} and Na^+ ions and the higher disorder expected for the bioglass series having mixed Na/Ca cationic environments; the combined effect of these factors is the shift of the Si-O-Si angle distribution to lower values due mainly to steric effects caused by the coexistence of Ca and Na ions in bioglasses. These factors lead to asymmetric profiles for the ν_s(Si-O-Si) Raman band, with its characteristic high-frequency tail, observed for the glass compositions considered in Fig. 1. Such Raman profiles reflect a broad distribution of the Si-O-Si bond angle, affected by the number of NBOs per silicate tetrahedron and by the different cationic environments in the vicinity of each NBO [51].

3.1.2. *High frequency Raman region*

Fig. 1 shows that the 800–1150 cm^{-1} Raman envelope involves more than three peaks. The peak at 948 cm^{-1} for 46S4 can be attributed to the symmetric stretching vibration of Q^2_{Si} tetrahedra involving mainly S-O$^-$ non-bridging bonds (O$^-$ = NBO), a 1080 cm^{-1} component and the 867 cm^{-1} band to the corresponding Q^3_{Si} and Q^1_{Si} vibrations respectively; while phosphate Q^0_P and Q^1_P units have also been postulated to contribute to the 800–1150 cm^{-1} envelope [43,44]. Raman spectroscopy shows also that longer annealing times (at temperatures 30 degrees below T_g) favor the formation of Q^2_{Si} units relative to Q^3_{Si} for samples 55S4.3 and 45S5 [43]. Comparison of the 60 and 55 mol% SiO_2 bioglass spectra and those of the 67 and 60 mol% SiO_2 binary Na-silicate glasses shows that the ca. 937 cm^{-1} band is stronger for the phosphorus containing bioglasses. This is a strong indication for the presence of Q^0_P orthophosphate tetrahedra, noting that the $\nu_1(Q^0_P)$ symmetric stretching band overlaps with the Q^2_{Si} band. In fact, this has already been observed in P_2O_5-containing silicate melts modified by sodium oxide (Q^0_P at ca. 935–940 cm^{-1} with ca. 25 cm^{-1} linewidth seen in Na-silicates containing 2–5 mol% P_2O_5 [53,54]) or calcium oxide (Q^0_P at ca. 970 cm^{-1} of ca. 25 cm^{-1} linewidth, with band height comparable to the Q^2_{Si} intensity seen in 0.46CaO-0.54SiO_2 containing 2.5 mol% P_2O_5 [55]). The signature of the pyrophosphate symmetric stretching vibration, $\nu_1(Q^1_P)$, is seen as a component at ca. 1000–1025 cm^{-1} that becomes more prominent in P_2O_5-containing Na-silicate glasses with higher modification [53,54] when compared to P_2O_5-containing Ca-silicates [55]. The above picture is further complicated by the presence of the two different cation modifiers, although the Na^+ and Ca^{2+} ion preferential coordination around silicate and phosphate tetrahedra is rather weak and essentially independent of the Si and P contents of the glass [56].

Even though the stretching of P-O$^-$ and Si-O$^-$ bonds in Q^n_P and Q^n_{Si} species does not involve directly the modifier cations, the stretching frequency depends on the electronic environment these cations provide, as this can change the degree of the ionic/covalent character of the oxygen-metal ion interactions and, consequently, the strength of the P-O$^-$ and Si-O$^-$ bonds. Table 3 lists Si-O$^-$ and P-O$^-$ stretching frequencies from Raman works on Na- and Ca-silicate glasses where it is seen that the frequencies may slightly depend on the modifier content and type. The Raman data could in principle be used to test the preferential coordination of the two modifier cations with the phosphate or silicate units in the glass. For example, for the Q^0_P units one could observe either one of two scenaria; (a) for a random distribution of Na/Ca ions at the nanoscale, the Q^0_P band would shift continuously in frequency depending on the relative Na_2O/CaO concentration (one-mode behavior), and (b) for a preferential coordination at the nanoscale, two Q^0_P bands would be seen at frequencies around 940 and 970 cm^{-1} corresponding to phosphate species charge-balanced by Na^+ and Ca^{2+} ions, respectively, with relative intensities proportional to the relative Na_2O/CaO concentration (two-mode behavior). For the lower total modifier content samples 60S3.8 and 55S4.3 the width of the ca. 937 cm^{-1} band in Fig. 1 is ca. 33 cm^{-1} and its line shape appears symmetric, pointing to a one-mode behavior, while its frequency is consistent with the presence of only Na^+ ion neighbors. For bioglasses 46S4 and 45S5 the situation is more complicated since the ca. 937 cm^{-1} band begins to upshift and/or broaden. The high frequency asymmetry of the band could be interpreted as a two-mode behavior for the orthophosphate band, but this is not certain since it overlaps with the Q^2_{Si} band.

A less uncertain conclusion can be reached by comparing the 46S4 and 45S5 bioglasses with a pure Ca phosphate-silicate glass CS0.85P8 of similar composition [55]. The profile similarity between 46S4 and CS0.85P8 glasses tends to support one-mode behavior for 46S4. As this glass composition includes twice as many Na^+ ions compared to Ca^{2+}, a random Na^+/Ca^{2+} mixing (66.7% Na^+ and 33.3% Ca^{2+}) would shift the Q^0_P band to ca. (2/3)*940 + (1/3)*968 = 949.3 cm^{-1}. Since the Q^0_P band is observed at ca. 948 cm^{-1} (Fig. 1) we have an indication that the phosphate part of the glass is preferentially coordinated by the neighboring Na^+ ions (84% Na^+ and 16% Ca^{2+}). Turning now our attention to the silicate species of the 46S4 sample, we note that the only species capable of offering an insight into the modifier preferential coordination is Q^1_{Si}, as it is the only one with Raman activity not overlapping with the phosphate bands [58]; Q^1_{Si} is seen at about 866 cm^{-1} in 46S4 which is practically identical to the Q^1_{Si} frequency in CaO-SiO_2 and distinctly

Table 3
Raman frequencies (in cm^{-1}) for the stretching $\nu(Si\text{-}O^-)$ and $\nu(P\text{-}O^-)$ in Q^n_{Si} or Q^n_P species in silicate[1] and phosphate-silicate[1] glasses with different degrees of modification.

Bonds Si-O^-, P-O^-	$\nu(Si\text{-}O^-)$ or $\nu(P\text{-}O^-)$ di- and quasi di-silicates					$\nu(Si\text{-}O^-)$ or $\nu(P\text{-}O^-)$ meta- and quasi meta-silicates			
	glass 1	glass 2	glass 3	glass 4	glass 5	glass 6	glass 7	glass 8	glass 9
$\nu(Si\text{-}O^-)$ in Q^1_{Si}	–	–	–	–	–	847–855	867	890	886
$\nu(Si\text{-}O^-)$ in Q^2_{Si}	942–945	958	–	950	950	970–985	962	973	975
$\nu(Si\text{-}O^-)$ in Q^3_{Si}	1095–1100	1057	1100	1100	1100	1060–1065	1050	1058	1066
$\nu(P\text{-}O^-)$ in Q^0_P	n/a	n/a	940	n/a	935	n/a		n/a	968
$\nu(P\text{-}O^-)$ in Q^1_P	n/a	n/a	1000	n/a	1025	n/a		n/a	–
references	[46,52]	[52]	[53]	[54]	[54]	[46,57]	[52]	[55]	[55]

[1] Glass compositions, (1): $0.33Na_2O\text{-}0.67SiO_2$; (2): $0.33CaO\text{-}0.67SiO_2$; (3): $0.10Na_2O\text{-}0.02P_2O_5\text{–}0.88SiO_2$; (4): $0.352Na_2O\text{-}0.004Al_2O_3\text{–}0.644SiO_2$; (5): $0.341Na_2O\text{-}0.003Al_2O_3\text{–}0.035P_2O_5\text{–}0.621SiO_2$; (6): $Na_2O\text{-}SiO_2$; (7): $CaO\text{-}SiO_2$; (8): $0.46CaO\text{-}0.54SiO_2$; (9): $0.450CaO\text{-}0.025P_2O_5\text{–}0.525SiO_2$.

away from 847 to 855 cm^{-1} seen in $Na_2O\text{-}SiO_2$ (see Table 3).

Summing up our conclusions on bioglass 46S4, the Raman data indicate that Q^0_P species are preferentially coordinated by Na^+ ions while the Q^1_{Si} species are preferentially coordinated by Ca^{2+} ions. Judging from the Raman data for 45S5 (Fig. 1) it is less clear which type of mode behavior is followed for this glass. However, the results of molecular-dynamics and NMR spectroscopy mentioned above [56] suggest a one-mode behavior with essentially randomized coordination around silicate and phosphate tetrahedra. Q^1_{Si} for this particular sample is seen active at 852 cm^{-1} which is in the range expected for $Na_2O\text{-}SiO_2$; clearly the preparation conditions can influence the Na^+/Ca^{2+} preferential coordination.

3.1.3. *Multiple peak fitting of the high frequency Raman region*

To explore further the nature of silicate and phosphate species present in bioglasses with different connectivity, we described the 800–1100 cm^{-1} Raman envelope with a superposition of Gaussian bands as shown in Fig. 3. By employing the minimum number of Gaussians, we find that at least 6 Gaussians are required for bioglasses with low connectivity (i.e., 46S4, 45S5), while 4 bands are sufficient for glasses of higher connectivity (i.e., 60S3.8, 55S4.3).

The proposed band assignment has been based on previous studies on silicate glasses [59,60], where the notation Q^{nm}_{Si} stands for a Q^n_{Si} tetrahedron connected to Q^m_{Si} tetrahedra, where n and m indicate the number of bridging oxygen atoms in the corresponding silicate tetrahedral units. The proposed assignments are shown in Table 4, and should be useful in gaining insights about the changes caused in the Raman spectra after electro-thermal poling.

Since the Raman activity of the Q^0_P and Q^2_{Si} species strongly overlap (Fig. 3), we started the fitting process from the binary system $xNa_2O\text{-}(1\text{–}x)SiO_2$ and used the derived linewidth values as fixed for fit of the Q_{Si} species in the spectra of the P_2O_5-containing bioglasses. The six rather closely spaced bands necessitate keeping more band linewidths and/or frequencies fixed during the fit, in order to get a reasonable variation of Raman band intensities as a function of network connectivity. To this aim, we have assigned the 1010–1030 cm^{-1} band to either (a) a combination of Q^{32}_{Si} and Q^1_P with equal weights when NC > 2.4 or to (b) a combination of Q^{23}_{Si} (Q^2_{Si} species cross-linking two disilicate structures) and Q^1_P with equal weights when NC ≤ 2.4, since using one peak for each species produced unstable fits. This approach is supported by results from a combination of classical and ab initio MD calculations [51] that show a bimodal behavior for the Q^2 band with one component overlapping with the Q^3 response. Therefore, a part of the intensity usually attributed to Q^3 should have been assigned to Q^2, and this is especially appropriate when the Q^2_{Si} are the majority species, i.e. for NC ≤ 2.4 (Fig. 3) or equivalently for $x > 0.444$ for binary alkali silicates.

We note at this point that, following earlier experimental observations [61], a number of authors have argued that the use of simple Gaussian functions for the fitting of the Raman response for the Q^n species is inadequate and that more complex functions [51] or Lorentzian dominated lineshapes [62] should be used. While we agree with these works, we believe that fitting a broad spectral region like the 800–1200 cm^{-1} envelope with >2–3 bands, like in the present case, produces similar band intensities using mixed Gaussian-Lorentzian lineshapes or simple Gaussians. We have tested this hypothesis with samples 46S4 (NC = 2.24) and 60S3.8 (NC = 3.02) as shown in Fig. 4a,b and 4c,d, respectively, where the high-frequency Raman envelop was fitted with (i) pure Gaussian bands (Fig. 4a,c), and (ii) pseudo-Voigt lineshapes with a 60% Lorentzian character for all the Q^n_{Si} species (Fig. 4b,d) as for Na-metasilicate glass [62]. The results in Fig. 4 show that the two fitting procedures give Q^n_{Si} integrated intensities differing by <0.5%.

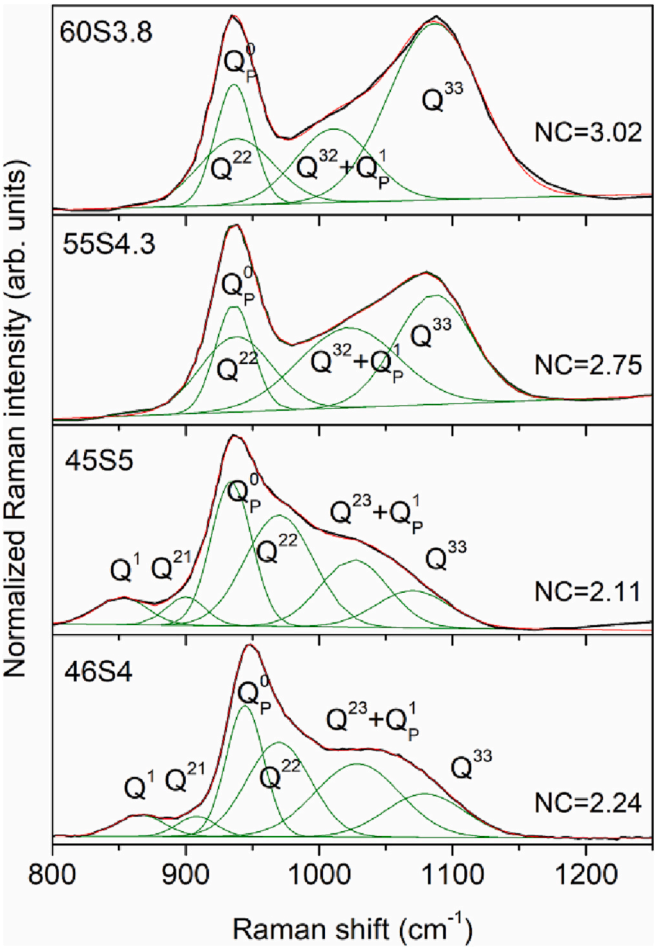

Fig. 3. Multiple peak fit with Gaussian bands of the high-frequency Raman region of bioglasses with different silicate connectivity, NC. See text and Table 4 for band assignments.

Table 4
Frequencies, bandwidths and assignments of bands used in this work in the high-frequency Raman envelope (800–1200 cm^{-1}) for bioglass 46S4 and other bioglasses of Table 2.

Frequency (cm^{-1})	Bandwidth (cm^{-1})	Assignment
1080–1090	~70	Si-O$^-$ stretch of Q^{33}_{Si}
1030	~75	(a) Q^{32}_{Si} and Q^{1}_{P} for NC > 2.4 or (b) Q^{23}_{Si} and Q^{1}_{P} for NC ≤ 2.4
935–970	~60	Si-O$^-$ stretch of Q^{22}_{Si} (partial overlap with Q^{31}_{Si}, 985–992 cm^{-1})
935–945	~33	P-O$^-$ stretch of Q^{0}_{P}
900–905	~35	Si-O$^-$ stretch of Q^{21}_{Si}
852–866		Si-O$^-$ stretch of Q^{1}_{Si}

Fig. 5a,b presents the results of Raman- and NMR-derived fractional populations of the various Q^{n}_{Si} units plotted against NC for bioglasses and Na-silicate glasses. The Raman results are from the present work, while the NMR fractions are from the literature [41,42]. As observed in Fig. 5, the network connectivity, NC, is a good parameter to probe the distribution of Q^{n}_{Si} species in different glass systems with or without phosphate content. Also, the Raman data are found in good agreement with the NMR data and this provides support to our Raman fitting and band assignments.

3.2. Electro-thermal poling induced structural rearrangements and chemical changes near the anodic surface in bioglass 46S4 and correlation with micro-SHG

Fig. 6 shows micro-Raman spectra measured along a line of the cross-section near the anode side of a freshly cut 46S4 sample after poling at 1500 V. The Raman spectrum of the pristine 46S4 glass (top spectrum of Fig. 6) has already been discussed in the presentation of Fig. 1 in section 3.1. As the Raman probe approaches the anode side of the poled 46S4 bioglass, the relative intensity of the band at ca. 1055 cm^{-1} increases with respect to that at 948 cm^{-1} and the 625 cm^{-1} band exhibits a progressive shift to lower frequency. Additionally, a new sharp peak at 1555 cm^{-1} and a broader envelope at ca. 1325 cm^{-1} (actually a doublet) emerge.

As a marker to track Raman changes after poling, we choose here the ca. 625 cm^{-1} band because its frequency ν_s(Si-O-Si) varies linearly with the silicate network connectivity, NC, as found in Fig. 2. Due to the asymmetry of this band, we have determined its frequency ν_s(Si-O-Si) and used it as an effective Raman marker of the poling-induced changes. For this we calculated the first derivative of the normalized Raman spectra using the Savitzky-Golay algorithm with 17-point smoothing, and determined the frequency value where the first derivative of the Raman intensity becomes zero. Fig. 7 demonstrates the procedure to obtain the frequency of the ca. 620 cm^{-1} band for the y = 0.5 and 6.0 μm Raman spectra of Fig. 6.

The obtained frequency ν_s(Si-O-Si) is shown in Fig. 8a as a function of distance from the anode side. The results show that the largest changes in ν_s(Si-O-Si) occurs directly under the anode, while spectra measured at distances greater than ca. 5 μm from the anode approach progressively that of the pristine glass (see Fig. 6).

The micro-SHG signal measured at the same position on the poled 46S4 glass cross section has been done using a parallel light polarizations configuration for both incident laser at 1064 nm and SHG signal at 532 nm, which were chosen to be perpendicular to the plane defined by the glass surface. Such experimental configuration allows probing the expected $\chi^{(2)}_{z,z,z}$ component induced along the applied poling field within the polarized anodic layer. The SHG intensity profile in Fig. 8b shows that a signal appears 1.0–1.5 μm below the anode surface and for a narrow depth range of ca. 3–4 μm. The rise of the SHG signal at 1.0–1.5 μm below the anode surface implies a positive charge density in this region, and the drop of the SHG signal at 3.5–6 μm indicates a negative charge density at the interface between the poled zone and the bulk glass. While a negative charge density at this interface has been discussed before [35], a model for explaining a positive charge density close to the anode does not exist to the best of our knowledge. Comparison of Fig. 8a and b shows that the micro-SHG signal develops deeper in the glass by ca. 1.5 μm than the poling-induced largest Raman

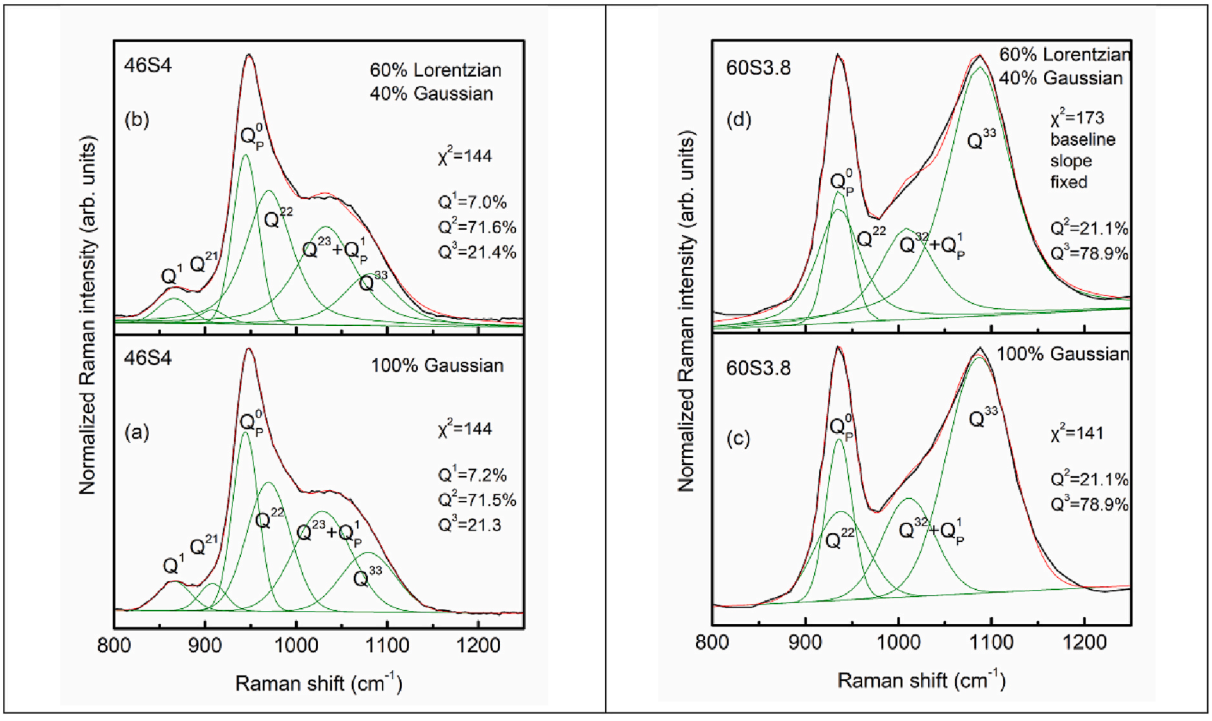

Fig. 4. Multiple peak fit of the high frequency region of the Raman spectra of bioglasses 46S4 (a,b) and 60S3.8 (c,d) with 100% Gaussian (a, c) or 60% Lorentzian–40% Gaussian (b, d) character.

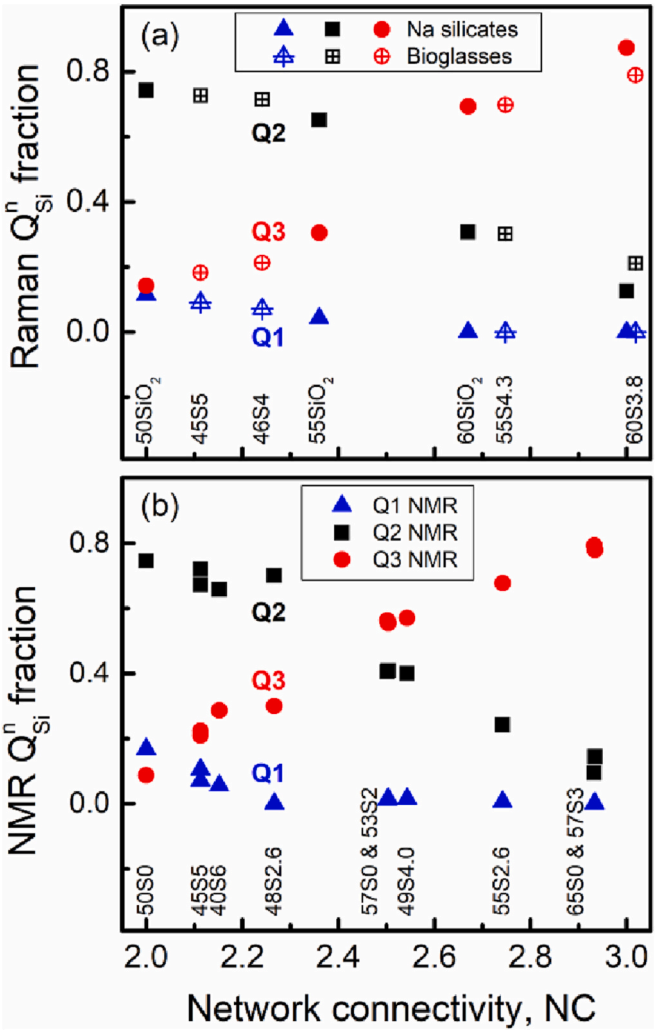

Fig. 5. Q^n_{Si} fractions in bioglasses and binary Na-silicate glasses of varying silicate connectivity, NC, as derived from the Raman analysis of this study (a), and from NMR spectroscopy (b) [41,42].

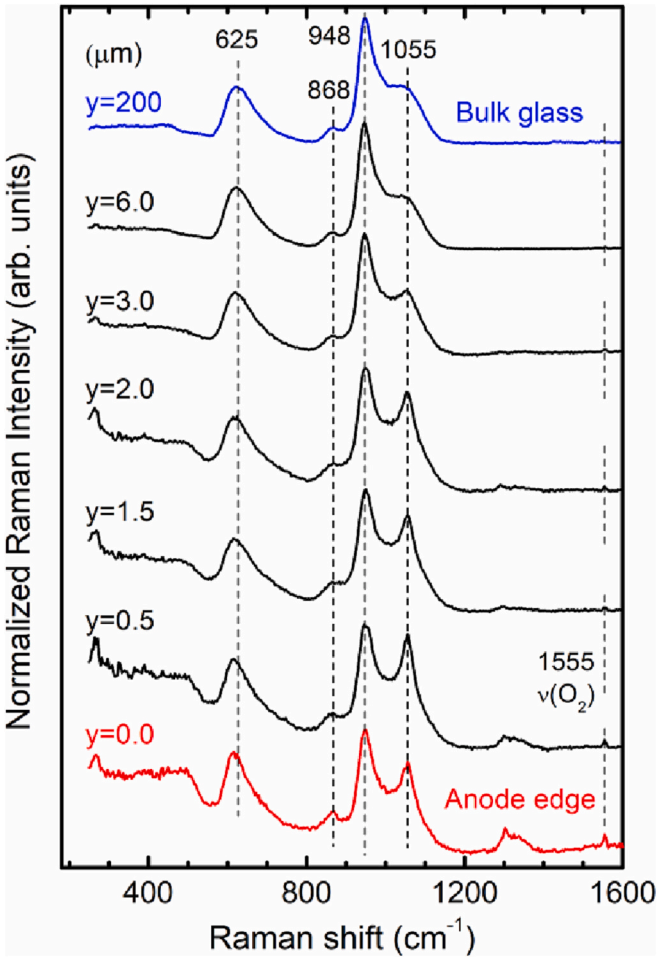

Fig. 6. Micro-Raman spectra measured after electro-thermal poling at the indicated distances from the anode edge (y = 0.0 μm), along the cross-section of a freshly cut 46S4 bioglass sample.

(structural) changes probed by the frequency of the ν_s(Si-O-Si) Raman mode.

As mentioned in the Introduction, the ETP mechanisms depend strongly on the electrode configuration which can vary between two extreme cases, namely from the fully blocking to the open (non-blocking) arrangement. The type of electrode influences the negative charge compensation mechanism which operates after charge dissociation, whereby the mobile cations migrate towards the cathode, forcing the negative space charge left close to the anode to be partially neutralized. In the present case, the Pt-sputtered electrodes for the ETP experiments on the bioglass 46S4 can be considered as fully blocking. In analogous instances of thermal poling, e.g., as in references [19, 20, 27], the very narrow Raman band measured at 1555 cm^{-1} close to the anode (Fig. 6) diminishes in intensity as one moves deeper into the bulk of the glass. This band is assigned to the stretching of molecular oxygen, $\nu(O_2)$, trapped close to the anode surface. The formation of molecular oxygen supports the oxide anion recombination and simultaneous electron hopping towards the anode region:

$$2(-O^-\ldots Na^+)\rightarrow(-O-)+O^{2-}+2Na^+ \quad (5a)$$

$$O^{2-}\rightarrow(1/2)O_2+2e^- \quad (5b)$$

Eq. (5a) describes the poling-induced creation of bridging oxygen (−O−) and oxide anion (O^{2-}); the oxidation of the latter leads to molecular oxygen formation and electron injection, Eq. (5b).

By using Eq. (4) established for bioglasses, we can convert the frequency values of the ν_s(Si-O-Si) band observed near the anode (Fig. 8a) to silicate network connectivity values. We note that the master curve for the bioglasses cannot be used directly, since the ν_s(Si-O-Si) Raman value corresponding to NC = 2.24 (i.e., the nominal value for 46S4) is 621.4 cm^{-1}, which differs by 3.6 cm^{-1} from the experimental value of 625.0 for this sample. We therefore adjust the intercept of the master curve by this amount, and use the same slope for sample 46S4 as presented by the red line in Fig. 2:

$$\nu_s(Si-O-Si) = 729.4 - 46.6\ NC \quad (6)$$

The estimated NC derived from the Raman data (Fig. 9a) is compared with the intensity of the $\nu(O_2)$ Raman band measured at 1555 cm^{-1} (Fig. 9b). The similar trends of the two curves supports the proposition that molecular oxygen formation is correlated with the glass connectivity increase at the anode side.

The change of slope in the variation of the ν_s(Si-O-Si) frequency or network connectivity as a function of depth from the anode seen to occur at 2.0–2.5 μm in Fig. 8a or Fig. 9a, necessitated the fitting of the asymmetric band centered at about 625 cm^{-1} to search for possible significant changes of the constituent peaks under the ca. 550–800 cm^{-1} Raman envelope. It was found that at least three Gaussian bands are required to give an acceptable fit of the envelope in question, with band frequencies, linewidths and amplitudes varying progressively over the sub-anodic distance covered. Characteristic fits are shown in Fig. 10 (left) for the 550–800 cm^{-1} envelopes corresponding to the pristine

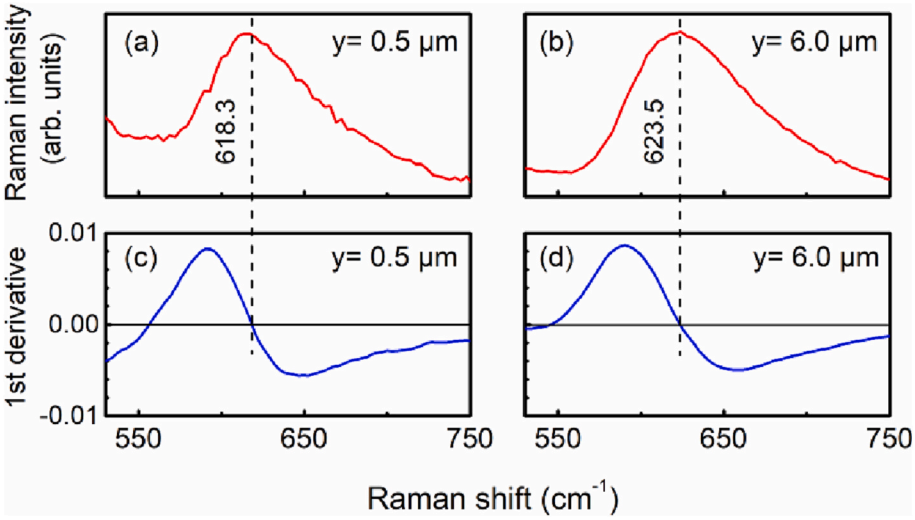

Fig. 7. Examples for the determination of the ν_s(Si-O-Si) frequency of the ca. 620 cm^{-1} band in the Raman spectra of Fig. 6 with y = 0.5 μm (a) and y = 6.0 μm (b). The ν_s(Si-O-Si) frequency is set as the point at which the first derivative of the Raman peak becomes zero in (c) and (d). See text for details.

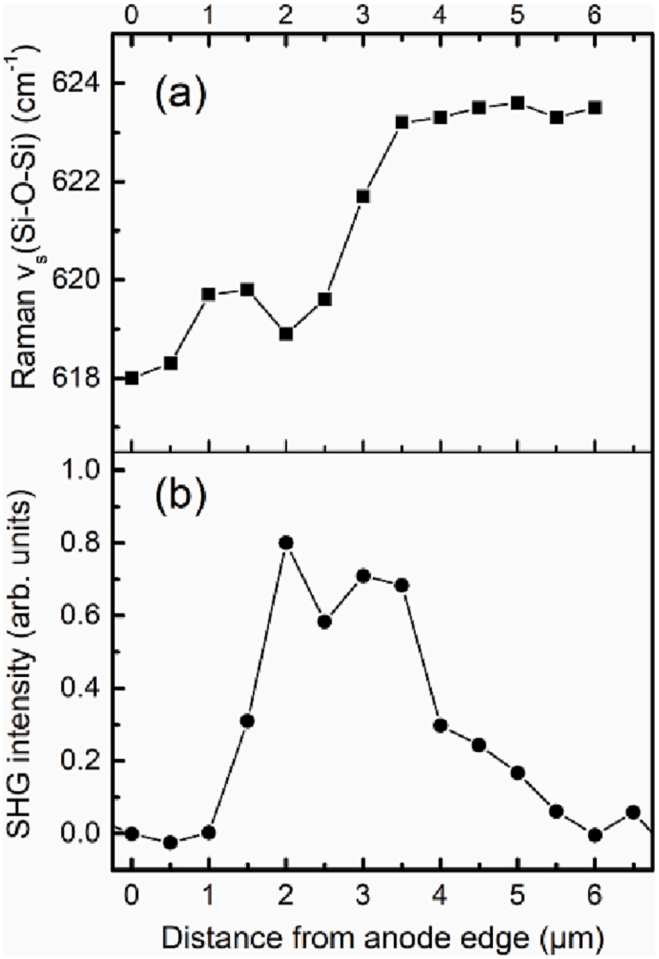

Fig. 8. Variation as a function of distance from the anode side (y = 0.0 μm) of (a) the ν_s(Si-O-Si) Raman frequency, and (b) the micro-SHG signal measured on the cross-section of the electro-thermally poled 46S4 bioglass.

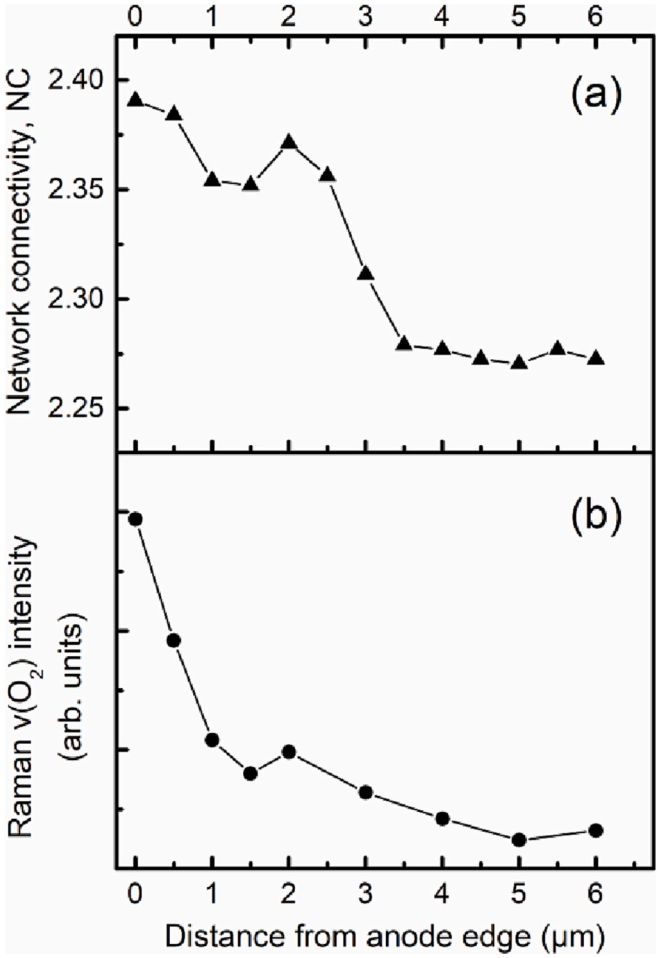

Fig. 9. Variation as a function of distance from the anode side (y = 0.0 μm) of (a) the silicate connectivity, NC, and (b) the corresponding $\nu(O_2)$ mode intensity measured on the cross-section of the electro-thermally poled 46S4 bioglass. The network connectivity was calculated from the ν_s(Si-O-Si) values using Eq. (6) for the particular 46S4 bioglass (see text for details).

46S4 samples and that measured after poling at 0.5 μm under the anode. As noted above, the asymmetric ν_s(Si-O-Si) Raman profile reflects a distribution of Si-O-Si bond angles, which is affected by the number of

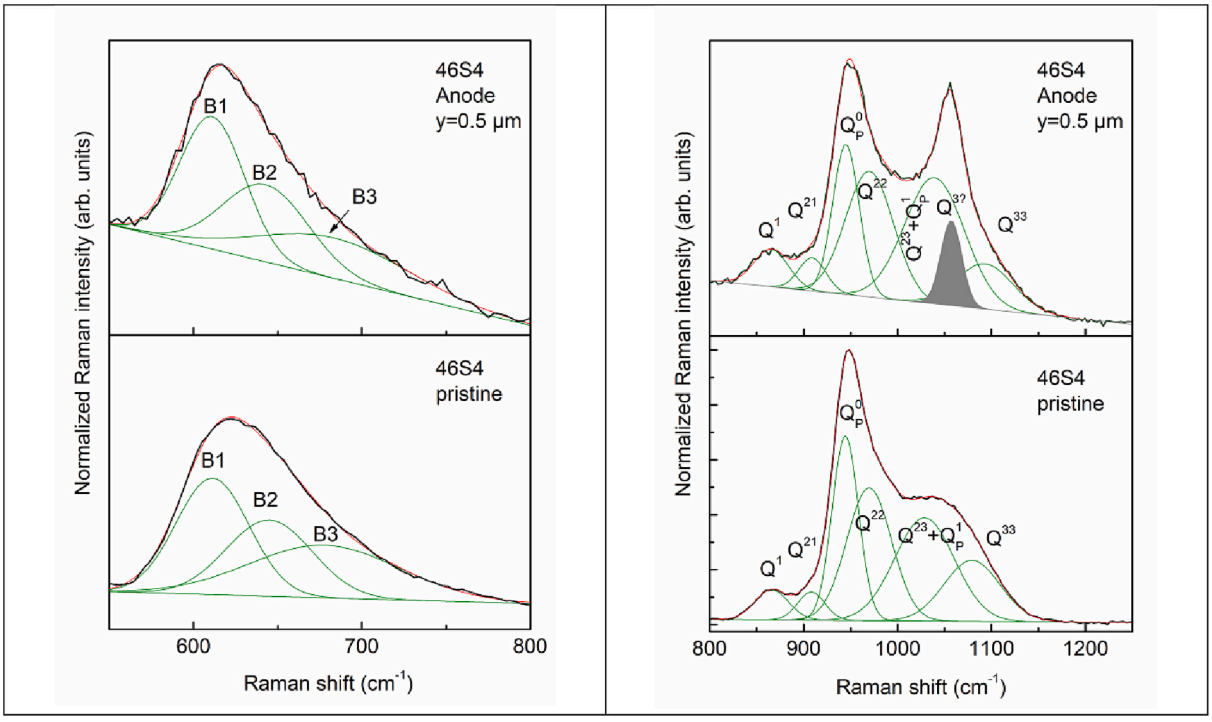

Fig. 10. Multiple peak fit of selected Raman regions of the pristine 46S4 glass and that measured after poling at 0.5 μm under the anode: (left) the ν_s(Si-O-Si) mode region, 550–800 cm^{-1}, and (right) the high frequency region, 800–1250 cm^{-1}. Band assignments are discussed in the text.

NBOs per Si and by the different cationic sites in the vicinity of each NBO [51], with the ν_s(Si-O-Si) frequency increasing upon increasing the number of NBOs. On this ground, we associate bands B1, B2 and B3 in Fig. 10(left) with Si-O-Si bridges having different cation environments, i.e. environments with one, two or more cation neighbors in the case of binary glasses, or environments with one Na (B1), one Ca (B2) or mixed Na/Ca neighbors (B3) for bioglasses.

The intensity of band B1 relative to the total intensity of the 550–800 cm^{-1} region is presented in Fig. 11a, where it is compared with the ratio of intensities of the bands for Q^3 (sum of intensities for Q^{33}_{Si} and Q^{32}_{Si} when NC > 2.4) and Q_2 (sum of intensities for Q^{21}_{Si}, Q^{22}_{Si} and Q^{23}_{Si} when NC ≤ 2.4) resulted from the fitting of the 800–1100 cm^{-1} envelope shown in Fig. 10 (right). If we associate band B1 with Si-O-Si bridges having one Na^+ ion in their vicinity, then the intensity reduction of B1 reflects the reduction of NBO population under the anode due to Na^+ ion migration. Then, association of band B2 with Si-O-Si bridges in the vicinity of a Ca^{2+} ion would be in agreement with Fig. 2 showing higher Raman shifts at least for the $45CaO\text{-}55SiO_2$ (vs. $45Na_2O\text{-}55SiO_2$) silicate glass, which has a connectivity value NC ~ 2.40 close to the 46S4 bioglass (NC = 2.24).

The ν_s(Si-O-Si) frequency values can be used to make a rough estimate of the average modifier concentration near the anode. Although the size of the laser spot is such that the Raman spectra at each given distance from the anode give only an average of the surrounding region, the frequency values of this band under the anode do not seem to support a complete depletion of Na^+ ions from the anode. A total Na^+ ion depletion would yield a glass composition close to the calcium disilicate which gives a band at ca. 590 cm^{-1} [52]; this is much lower than the values observed, 618–625 cm^{-1}. Also, a Na^+ ion retention only for the charge-balancing needs of the orthophosphate species would again give a Ca-silicate composition close to the disilicate with ν_s(Si-O-Si) close to 590 cm^{-1}. The above scenaria would correspond to connectivity values of 3.33 and 2.91, respectively, both being much higher than the estimated NC value below the anode, NC = 2.37 (see Table 5 and Fig. 9a). Instead, the data show a maximum Na^+ ion depletion of the order of 12% in the Raman-probed anode area relative to the pristine bioglass

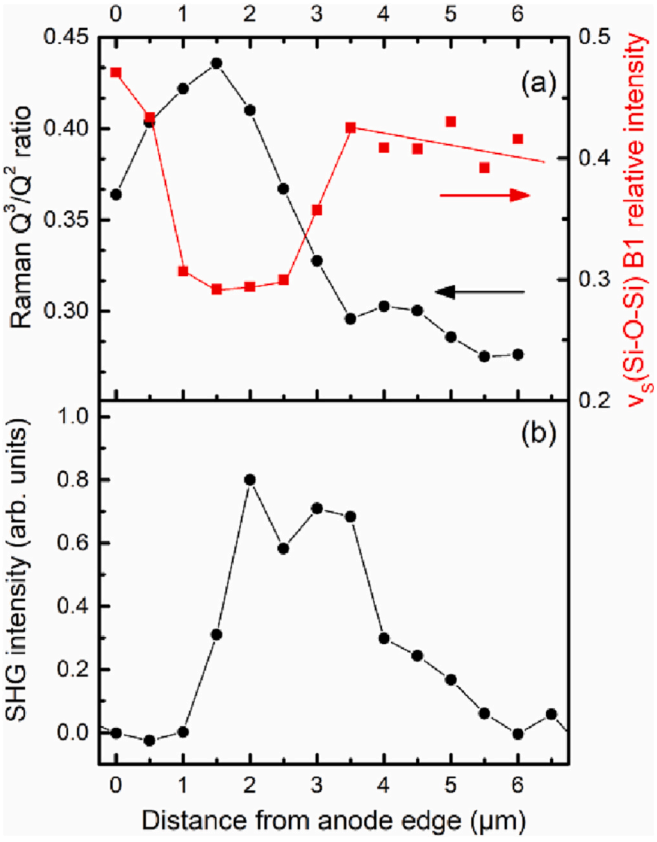

Fig. 11. Relative intensity of band B1 and of the Q^3_{Si}/Q^2_{Si} intensity ratio as a function of distance from the anode edge after poling (a), in comparison with the measured SHG signal (b) (as in Fig. 8b).

Table 5
Anode glass composition vs. network connectivity for different scenaria of Na ion migration from the anode side induced by electro-thermal poling.

Scenario	Composition (mol)	NC	Reduction of Na^+ amount
All Na^+ has left anode	0.337 CaO-0.043 P_2O_5–0.620 SiO_2	3.33	100%
All Na^+ has left anode, but for Na^+ charge-balancing the orthophosphate units	0.114Na_2O-0.299CaO-0.038P_2O_5–0.550SiO_2	2.91	54.8%
Some Na^+ ions move and the connectivity at the anode reaches NC = 2.40	0.223Na_2O-0.262CaO-0.033P_2O_5–0.482SiO_2	2.40	11.5%

concentration – see Table 5.

Comparison of Figs. 8b and 9a shows that the glass connectivity increases in the region close to the anode in a layer <1 μm thick, where no SHG signal has been detected. The SHG-active region is measured at intermediate network connectivity values and exhibits its maximum responses in the sub-anodic region extending from about 1.5 to 4.0 μm (Fig. 8b). Thus, the positive charge density located around 1–1.5 μm under anode correlates with a Q^3_{Si}/Q^2_{Si} maximum in this region (Fig. 11a), suggesting that more cations are present than needed for the compensation of Q^3_{Si} and the Q^2_{Si} units. A possible reason is that close to the Pt electrode, electrons are transported faster towards the electrode than Na^+ ions towards the opposite direction. At fields close to the breakdown field, this seems feasible.

The fitting of the 800–1200 cm^{-1} envelope may also be used to track the Raman changes in the sub-anodic layer. In this case we observe a new rather narrow band emerging at ca. 1057 cm^{-1} – a typical example is shown at the top of Fig. 10(right). In Fig. 11a we additionally plot the variation of the Q^3/Q^2 relative intensity ratio, by adding the ca. 1057 cm^{-1} band intensity to the Q^3_{Si} species and excluding, of course, the Q^0_P and Q^1_P bands. If we attribute the 1057 cm^{-1} band to new more ordered Q^3_{Si} species (e.g., related to the observed Ca pile-up layer), we can again convert the observed population increase of species with more bridging oxygen atoms to an increased network connectivity. The fact that the relative intensity Q^3/Q^2 shows a maximum when the ν_s(Si-O-Si) band #1 intensity shows a minimum with a small depth shift (Fig. 11a), points to a direct correlation between these two quantities. The diminution of the relative intensity of the Q^2 band close to the anode surface serves also the scenario of augmented connectivity (Fig. 9a).

Next, we examine the possibility of attributing the ca. 1057 cm^{-1} band to the symmetric stretching of the PO_3^{2-} unit of the Q^1_P pyrophosphate species in a richer Ca environment (Ca-pyrophosphate, 67CaO-33P_2O_5 or $Ca_2P_2O_7$) as a result of the field-assisted Na^+ ion migration (although the Na^+ charge-balancing orthophosphate species would be expected to be less mobile than the silicate network Na^+ ions). Poling-induced pyrophosphate formation would contribute to increased connectivity of the phosphate rather than the silicate network. However, the frequency of 1057 cm^{-1} is considerably higher than the $\nu(PO_3^{2-})$ frequency reported for amorphous Ca-pyrophosphate at ca. 1026 cm^{-1} [63]).

While the results presented above concern measurements along lines perpendicular to the anode surface (i.e., linescans), Raman and SHG maps can be generated by scanning sample areas. Such maps are shown in Fig. 12 and verify the presence of a SHG-inactive layer of 1.0–1.5 μm thickness below the anode, while the thickness of the SHG-active layer is of the order of 2.0–2.5 μm. At the same time, the Raman structural changes, as determined by the ν_s(Si-O-Si) frequency, appear strongest directly under the anode (Fig. 12(left)) and, thus, they precede the formation of the optically non-linear layer (Fig. 12(right)). It is noted that a similar situation was reported for ETP poled soda-lime glass [64], where the maximum of the SHG signal was measured at ca. 1.5 μm under the anode. Under the assumption that the observed SHG signal is originating from the interaction of a static electric field and the glass third order optical susceptibility, these results denote the location of an ETP-induced space charge at the transition between the depletion layer and the non-affected bulk glass. In the maps of Fig. 12, we observe that the strongest SHG signal is not detected for areas with the most intense preceding silicate network Raman changes, but rather for areas with modest preceding silicate network Raman changes with respect to the pristine 46S4 bioglass. It is conceivable that this behavior may be characteristic of a wider class of thermally poled glasses.

To explain such observations, one should take into account the complex change in the dielectric properties of the polarized glass matrix determining the final charge distribution. We note that for such an ionic glass composition, ETP is known to induce (i) strong modifications of the dielectric properties, especially linked to a decrease of the ionic charge carriers but also to significant density variations [65,66], and (ii) a multilayer configuration due to the large mobility difference of alkali and alkaline earth cations involved in the polarization process, thus creating a complex succession of depletion and stacking layers [37].

Detailed dielectric characterization of such a multilayer system is necessary to predict accurately the space charge strength and location, which is out of the objectives of the current study. Nevertheless, we point out that correlative Raman/SHG data demonstrate that the induced connectivity changes influence directly the strength of the frozen electric field. Such a correlative experimental approach could help to quantify these effects at the microscale level, but this requires a

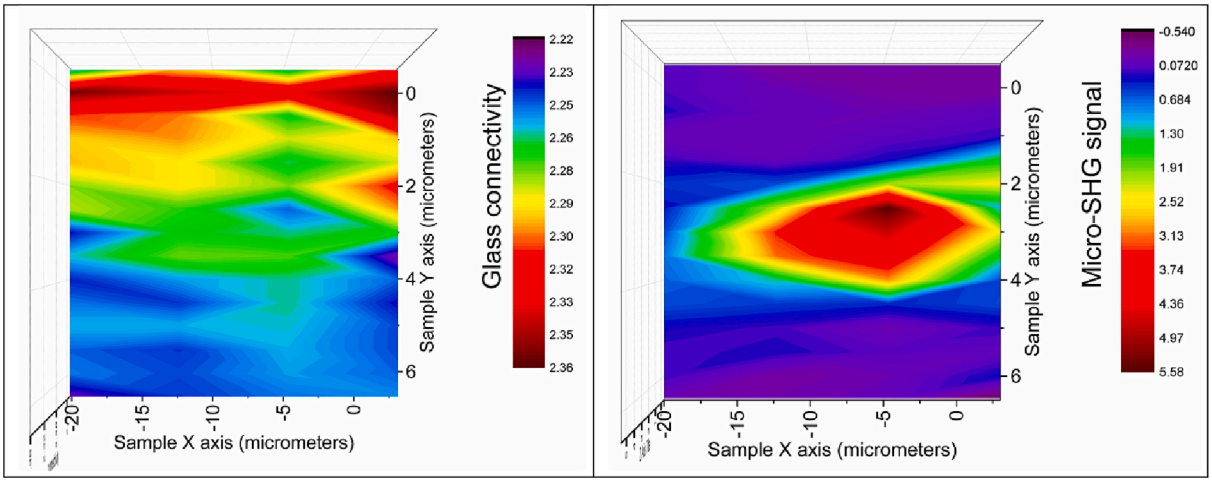

Fig. 12. Correlation between maps of network connectivity, NC, estimated from the Raman frequency v_s(Si-O-Si) (left), and SHG intensity (right) obtained from a freshly cut area of the electro-thermally poled 46S4 bioglass. Note that y = 0 μm corresponds to the anode side of the poled bioglass sample.

very accurate link between structural variations and dielectric properties.

4. Conclusions

Motivated by the application of electro-thermal poling (ETP) to enhance the activity of bioglasses, we have studied in this work the effect of ETP on the structure and second harmonic generation (SHG) in the bioglass 46S4 (25.2Na_2O-25.2CaO-3.2P_2O_5–46.4SiO_2, mol%). The understanding of the poling-induced changes in the structure of 46S4 was based on a systematic comparison of the Raman spectra of binary Na- and Ca-silicate glasses and phosphate-silicate bioglasses with silicate network connectivity in the range NC = 2.0–3.0. This approach involved multiple peak fitting of the high-frequency Raman region (800–1200 cm^{-1}) and the assignment of the resulted component bands to silicate (Q^n_{Si}) and phosphate (Q^n_P) tetrahedral units with n bridging-oxygen atoms per unit. The Raman derived population of Q^n species was correlated with the network connectivity and was found to agree well with available NMR data on analogous glasses. This analysis showed also that the Q^3_{Si}/Q^2_{Si} intensity ratio after electro-thermal poling varies as a function of distance from the anode and exhibits its maximum value in the range of 1–2 μm below the anode.

Further quantification of the poling-induced structural changes was based on the frequency ν_s(Si-O-Si) of the Raman peak at ca. 625 cm^{-1}, due to the symmetric stretching-bending vibration of the Si-O-Si bridges, since ν_s(Si-O-Si) and NC were found to be linearly correlated in silicate glass systems. The depth-dependence of the structural changes in the sub-anodic region of thermally poled 46S4 was registered by ν_s(Si-O-Si) and found to reflect a stepwise increase of the silicate network connectivity, with NC reaching 2.37 at the anode.

Raman evidence was found for molecular oxygen formation as a result of ETP on 46S4, which suggests oxidation of oxide ions migrating or recombining together with concomitant electron hopping towards the anode. The charge compensation scheme proposed to counterbalance Na^+ migration from the anode cannot estimate the proportion of anionic and electronic conductivity contributing to the poling mechanism.

The SHG-active layer is about 4.5 μm thick and is preceded by a 1.0 μm thick NLO-inactive layer, which develops right under the anode. This implies a positive charge density located at about 1.0 μm under the anode, and a negative charge density at the interface between the poled zone and the bulk glass. The positive charge density located around 1 μm under anode correlates with a Q^3_{Si}/Q^2_{Si} maximum in this region, implying an increasing network connectivity and suggesting that more Na^+ ions are located here than needed for the compensation of the negatively charged Q^3_{Si} and Q^2_{Si} units.

CRediT authorship contribution statement

D. Palles: Investigation, Data curation, Formal analysis, Writing – original draft, Writing – review & editing. **M. Dussauze:** Investigation, Writing – review & editing. **C.R. Mariappan:** Investigation. **V. Rodriguez:** Writing – review & editing. **B. Roling:** Writing – review & editing. **E.I. Kamitsos:** Conceptualization, Formal analysis, Writing – original draft, Writing – review & editing, Funding acquisition, Supervision.

Declaration of Competing Interest

The authors declare that they have no known competing financial interests or personal relationships that could have appeared to influence the work reported in this paper.

Data availability

The data that support the findings of this study are available from the corresponding author upon reasonable request.

Acknowledgments

We gratefully acknowledge partial support of this work by the EC / Marie Curie Actions program (Grant No. MTKD-CT-2006-042301).

References

[1] R.A. Myers, N. Mukherjee, S.R.J. Brueck, Large second-order nonlinearity in poled fused silica, Opt. Lett. 16 (1991) 1732–1734.
[2] M. Dussauze, T. Cremoux, F. Adamietz, V. Rodriguez, E. Fargin, G. Yang, T. Cardinal, Thermal poling of optical glasses: mechanisms and second-order optical properties, Int. J. Appl. Glass Sci. 3 (2012) 309–320.
[3] L. Karam, F. Adamietz, D. Michau, C. Gonçalves, M. Kang, R. Sharma, G. S. Murugan, T. Cardinal, E. Fargin, V. Rodriguez, K.A. Richardson, M. Dussauze, Electrically micro-polarized amorphous Sodo-niobate film competing with crystalline lithium niobate second order optical response, Adv. Opt. Mater. 8 (2020) 2000202.
[4] L. Wang, Y. He, Z. Zhan, L. Yu, H. Wang, D. Chen, A novel sacrificial-layer process based on anodic bonding and its application in an accelerometer, AIP Adv. 5 (2015), 041323.
[5] K. Yamashita, N. Oikawa, T. Umegaki, Acceleration and deceleration of bone-like crystal growth on ceramic hydroxyapatite by electric poling, Chem. Mater. 8 (1996) 2697–2700.
[6] A. Obata, S. Nakamura, Y. Moriyoshi, K. Yamashita, Electrical polarization of bioactive glass and assessment of their in vitro apatite deposition, J. Biomed. Mater. Res. 67A (2003) 413–420.
[7] A. Obata, S. Nakamura, K. Yamashita, Interpretation of electrical polarization and depolarization mechanisms of bioactive glasses in relation to ionic migration, Biomaterials 25 (2004) 5163–5169.
[8] C.R. Mariappan, D.M. Yunos, A.R. Boccaccini, B. Roling, Bioactivity of electro-thermally poled bioactive silicate glass, Acta Biomater. 5 (2009) 1274–1283.
[9] A.A. Lipovskii, V.G. Melehin, M.I. Petrov, Yu.P. Svirko, Thermal electric field imprinting lithography: fundamentals and applications, in: T.C. Hennesy (Ed.), Lithography: Principles, Processes and Materials, Nova Science Publisher Inc, New-York, 2011, pp. 149–163.
[10] R. Alvarado, L. Karam, R. Dahmani, A. Lepicard, F. Calzavara, A. Piarristeguy, A. Pradel, T. Cardinal, F. Adamietz, E. Fargin, M. Chazot, K. Richardson, L. Vellutini, M. Dussauze, Patterning of the surface electrical potential on chalcogenide glasses by a thermoelectrical imprinting process, J. Phys. Chem. C 124 (2020) 23150–23157.
[11] C. McLaren, W. Heffner, R. Tessarollo, R. Raj, H. Jain, Electric field-induced softening of alkali silicate glasses, Appl. Phys. Lett. 107 (2015), 184101.
[12] C. McLaren, B. Roling, R. Raj, H. Jain, Mechanism of electric field-induced softening (EFIS) of alkali silicate glasses, J. Non-Cryst. Solids 471 (2017) 384–395.
[13] F. Lind, D. Palles, D. Möncke, E.I. Kamitsos, L. Wondraczek, Modifying the surface wetting behavior of soda lime silicate glass substrates through thermal poling, J. Non-Cryst. Solids 462 (2017) 47–50.
[14] A. Lepicard, T. Cardinal, E. Fargin, F. Adamietz, V. Rodriguez, K. Richardson, M. Dussauze, Surface reactivity control of a borosilicate glass using thermal poling, J. Phys. Chem. C 119 (2015) 22999–23007.
[15] A. Goillot, A. Maillard, T. Galstian, Y. Messaddeq, F. Adamietz, V. Rodriguez, M. Dussauze, Plasma assisted micro poling of glassy surfaces: a new tool to achieve liquid crystal multi-domain alignments [invited], Opt. Mater. Express 12 (2022) 2462–24731.
[16] J. Luo, S. Bae, M. Yuan, E. Schneider, M.T. Lanagan, C.G. Pantano, S.H. Kim, Chemical structure and mechanical properties of soda lime silica glass surfaces treated by thermal poling in inert and reactive ambient gases, J. Am. Ceram. Soc. 101 (2018) 2951–2964.
[17] M. Chazot, M. Paraillous, S. Jouannigot, L. Teulé-Gay, J.-P. Salvetat, F. Adamietz, R. Alvarado-Meza, L. Karam, A. Poulon, T. Cardinal, E. Fargin, M. Dussauze, Enhancement of mechanical properties and chemical durability of soda-lime silicate glasses treated by DC gas discharges, J. Am. Ceram. Soc. 104 (2021) 157–166.
[18] P. Pernice, A. Paleari, M. Ferraris, M. Fokine, E. Fanelli, R. Lorenzi, G. Spinolo, A. Aronne, Electric field induced structural modification and second order optical nonlinearity in potassium niobium silicate glass, J. Non-Cryst. Solids 355 (2009) 2578–2582.
[19] M. Dussauze, V. Rodriguez, A. Lipovskii, M. Petrov, C. Smith, K. Richardson, T. Cardinal, E. Fargin, E.I. Kamitsos, How does thermal poling affect the structure of soda-lime glass? J. Phys. Chem. C 114 (2010) 12754–12759.
[20] A.V. Redkov, V.G. Melehin, V.V. Statcenko, A.A. Lipovskii, Nanoprofiling of alkali-silicate glasses by thermal poling, J. Non-Cryst. Solids 409 (2015) 166–169.
[21] A.V. Redkov, V.G. Melehin, A.A. Lipovskii, How does thermal poling produce interstitial molecular oxygen in silicate glasses? J. Phys. Chem. C 119 (2015) 17298–17307.
[22] D. Möncke, M. Dussauze, E.I. Kamitsos, C.P.E. Varsamis, D. Ehrt, Thermal poling induced structural changes in sodium borosilicate glasses, Phys. Chem. Glasses Eur. J. Glass Sci. Technol. B 50 (2009) 229–235.
[23] N.J. Smith, C.G. Pantano, Structural and compositional modification of a barium boroaluminosilicate glass surface by thermal poling, Appl. Phys. A – Mater. Sci. Process. 116 (2014) 529–543.
[24] C. Corbari, L.C. Ajitdoss, I.C.S. Carvalho, O. Deparis, F.P. Mezzapesa, P. G. Kazansky, K. Sakaguchi, The problem of achieving high second-order

nonlinearities in glasses: the role of electronic conductivity in poling of high index glasses, J. Non-Cryst. Solids 356 (2010) 2742–2749.
[25] M. Dussauze, E.I. Kamitsos, E. Fargin, V. Rodriguez, Structural rearrangements and second-order optical response in the space charge layer of thermally poled sodium-niobium borophosphate glasses, J. Phys. Chem. C 111 (2007) 14560–14566.
[26] M. Dussauze, V. Rodriguez, L. Velli, C.P.E. Varsamis, E.I. Kamitsos, Polarization mechanisms and structural rearrangements in thermally poled sodium-alumino phosphate glasses, J. Appl. Phys. 107 (2010), 043505-1 to 6.
[27] G. Guimbretiere, M. Dussauze, V. Rodriguez, E.I. Kamitsos, Correlation between second-order optical response and structure in thermally poled sodium niobium-germanate glass, Appl. Phys. Lett. 97 (2010), 171103-1 to 3.
[28] D.E. Carlson, K.W. Hang, G.F. Stockdale, Electrode "polarization" in alkali-containing glasses, J. Am. Ceram. Soc. 55 (1972) 337–341.
[29] D.E. Carlson, Ion depletion of glass at a blocking anode: I, theory and experimental results, J. Am. Ceram. Soc. 57 (1974) 291–294.
[30] D.E. Carlson, K.W. Hang, G.F. Stockdale, Ion depletion of glass at a blocking anode: II, properties of ion-depleted glasses, J. Am. Ceram. Soc. 57 (1974) 295–300.
[31] D.E. Carlson, Anodic proton injection in glasses, J. Am. Ceram. Soc. 57 (1974) 461–466.
[32] A. Tandia, M. Reveil, K. Deenamma Vargheese, J. Luo, J.C. Mauro, P. Clancy, Modeling the thermal poling of glasses using molecular dynamics. Part 1: Effects on glass structure, J. Non-Cryst. Solids 461 (2017) 98–103.
[33] M. Reveil, A. Tandia, J. Luo, K. Deenamma Vargheese, S. Goyal, J.C. Mauro, P. Clancy, Modeling the thermal poling of glasses using molecular dynamics. Part 2: effects on elastic properties, J. Non-Cryst. Solids 468 (2017) 17–26.
[34] A. Vegiri, E.I. Kamitsos, Molecular dynamics study of structural reorganization by electro-thermal poling in sodium diborate glass, J. Non-Cryst. Solids 472 (2017) 14–24.
[35] C.R. Mariappan, B. Roling, Investigation of bioglass–electrode interfaces after thermal poling, Solid State Ionics 179 (2008) 671–677.
[36] C.R. Mariappan, B. Roling, Mechanism and kinetics of Na^+ ion depletion under the anode during electro-thermal poling of a bioactive glass, J. Non-Cryst. Solids 356 (2010) 720–724.
[37] J. Zakel, M. Balabajew, B. Roling, On the mechanism of field-induced mixed ionic–electronic transport during electro-thermal poling of a bioactive sodium–calcium phosphosilicate glass, Solid State Ionics 265 (2014) 1–6.
[38] V. Rodriguez, D. Talaga, F. Adamietz, J.L. Bruneel, M. Couzi, Hyper-Raman macro- and micro-spectroscopy in materials: towards high quality signals and good spatial resolution, Chem. Phys. Lett. 431 (2006) 190–194.
[39] J.A. Duffy, M.D. Ingram, Establishment of an optical scale for Lewis basicity in inorganic oxyacids, molten salts, and glasses, J. Am. Chem. Soc. 93 (1971) 6448–6454,. J.A. Duffy, M.D. Ingram, An interpretation of glass chemistry in terms of the optical basicity concept, J. Non-Cryst. Solids 21 (1976) 373–410.
[40] D.S. Brauer, D. Möncke, Chapter 3 – Introduction to the structure of silicate, phosphate and borate glasses, in: A.R. Boccaccini, D.S. Brauer, L. Hupa (Eds.), RSC Smart Materials No 23 – Bioactive Glasses: Fundamentals, Technology and Applications, The Royal Society of Chemistry Publisher, 2017, pp. 61–88.
[41] A. Pedone, T. Charpentier, G. Malavasi, M.C. Menziani, New insights into the atomic structure of 45S5 bioglass by means of solid-state NMR spectroscopy and accurate first-principles simulations, Chem. Mater. 22 (2010) 5644–5652.
[42] Y. Yu, M. Edén, Structure–composition relationships of bioactive borophosphosilicate glasses probed by multinuclear ^{11}B, ^{29}Si, and ^{31}P solid state NMR, RSC Adv. 6 (2016) 101288–101303,. R. Mathew, B. Stevensson, A. Tilocca, and M. Edén, toward a rational design of bioactive glasses with optimal structural features: composition-structure correlations unveiled by solid-state NMR and MD simulations, J. Phys. Chem. B 118 (2014) 833–844.
[43] S. Murugavel, C. Vaid, V.S. Bhadram, C. Narayana, Ion transport mechanism in glasses: non-Arrhenius conductivity and non-universal features, J. Phys. Chem. B 114 (2010) 13381–13385.
[44] C.C. Lin, L.C. Huang, P. Shen, $Na_2CaSi_2O_6$–P_2O_5 based bioactive glasses. Part 1: elasticity and structure, J. Non-Cryst. Solids 351 (2005) 3195–3203.
[45] J.A. Kapoutsis, PhD Thesis. National and Kapodistrian University of Athens, 1998.
[46] S. Brawer, W. White, Raman spectroscopic investigation of the structure of silicate glasses. I. the binary alkali silicates, J. Chem. Phys. 63 (1975) 2421–2432.
[47] P. González, J. Serra, S. Liste, S. Chiussi, B. León, M. Pérez-Amor, Raman spectroscopic study of bioactive silica based glasses, J. Non-Cryst. Solids 320 (2003) 92–99.
[48] L. Marsich, L. Moimas, V. Sergo, C. Schmid, Raman spectroscopic study of bioactive silica-based glasses: the role of the alkali/alkali earth ratio on the non-bridging oxygen/bridging oxygen (NBO/BO) ratio, Spectroscopy 23 (2009) 227–232.
[49] T. Furukawa, K.E. Fox, W.B. White, Raman spectroscopic investigation of the structure of silicate glasses. III. Raman intensities and structural units in sodium silicate glasses, J. Chem. Phys. 75 (1981) 3226–3237.
[50] E.I. Kamitsos, J.A. Kapoutsis, H. Jain, C.H. Hsieh, Vibrational study of the role of trivalent ions in sodium trisilicate glass, J. Non-Cryst. Solids 171 (1994) 31–45.
[51] D. Kilymis, S. Ispas, B. Hehlen, S. Peuget, J.-M. Delaye, Vibrational properties of sodosilicate glasses from first-principles calculations, Phys. Rev. B 99 (2019), 054209-1 to 14.
[52] B. Mysen, D. Virgo, C.M. Scarfe, Relations between the anionic structure and viscosity of silicate melts – a Raman spectroscopic study, Am. Mineral. 65 (1980) 690–710.
[53] B. Mysen, Phosphorus speciation changes across the glass transition in highly polymerized alkali silicate glasses and melts, Am. Mineral. 81 (1996) 1531–1534.
[54] M.J. Toplis, B. Reynard, Temperature and time-dependent changes of structure in phosphorus containing aluminosilicate liquids and glasses: in situ Raman spectroscopy at high temperature, J. Non-Cryst. Solids 263&264 (2000) 123–131.
[55] B. Mysen, Iron and phosphorus in calcium silicate quenched melts, Chem. Geol. 98 (1992) 175–202.
[56] R. Mathew, B. Stevensson, M. Edén, Na/ca intermixing around silicate and phosphate groups in bioactive phosphosilicate glasses revealed by heteronuclear solid-state NMR and molecular dynamics simulations, J. Phys. Chem. B 119 (2015) 5701–5715.
[57] B. Mysen, F.J. Ryerson, D. Virgo, The structural role of phosphorus in silicate melts, Am. Mineral. 66 (1981) 106–117.
[58] H.W. Nesbitt, G.M. Bancroft, G.S. Henderson, P. Richet, C. O'Shaughnessy, Melting, crystallization, and the glass transition: toward a unified description for silicate phase transitions, Am. Mineral. 102 (2017) 412–420.
[59] O.N. Koroleva, V.N. Anfilogov, A. Shatskiy, K.D. Litasov, Structure of Na_2O–SiO_2 melt as a function of composition: in situ Raman spectroscopic study, J. Non-Cryst. Solids 375 (2013) 62–68.
[60] E. Stavrou, D. Palles, E.I. Kamitsos, A. Lipovskii, D. Tagantsev, Y. Svirko, S. Honkanen, Vibrational study of thermally ion-exchanged sodium aluminoborosilicate glasses, J. Non-Cryst. Solids 401 (2014) 232–236.
[61] E.I. Kamitsos, W.M. Risen, Vibrational spectra of single and mixed alkali pentasilicate glasses, J. Non-Cryst. Solids 65 (1984) 333–354.
[62] G.M. Bancroft, H.W. Nesbitt, G.S. Henderson, C. O'Shaughnessy, A.C. Withers, D. R. Neuville, Lorentzian dominated lineshapes and linewidths for Raman symmetric stretch peaks (800–1200 cm^{-1}) in Qn (n=1–3) species of alkali silicate glasses/melts, J. Non-Cryst. Solids 484 (2018) 72–83.
[63] J.E. Pemberton, L. Latifzadeh, J.P. Fletcher, S.H. Risbud, Raman spectroscopy of calcium phosphate glasses with varying CaO modifier concentrations, Chem. Mater. 3 (1991) 195–200.
[64] H. An, S. Fleming, Second-order optical nonlinearity and accompanying near-surface structural modifications in thermally poled soda-lime silicate glasses, J. Opt. Soc. Am. B 23 (2006) 2303–2309.
[65] L. Karam, F. Adamietz, V. Rodriguez, F. Bondu, A. Lepicard, T. Cardinal, E. Fargin, K. Richardson, M. Dussauze, The effect of the sodium content on the structure and the optical properties of thermally poled sodium and niobium borophosphate glasses, J. Appl. Phys. 128 (2020), 043106.
[66] M. Dussauze, E.I. Kamitsos, E. Fargin, V. Rodriguez, Refractive index distribution in the nonlinear optical layer of thermally poled oxide glasses, Chem. Phys. Lett. 470 (2009) 63–66.